

This work has been submitted to the IEEE for possible publication. Copyright may be transferred without notice, after which this version may no longer be accessible.

EKF-Based Radar-Inertial Odometry with Online Temporal Calibration

Changseung Kim¹, Geunsik Bae¹, Woojae Shin¹, Sen Wang², and Hyondong Oh¹

Abstract—Accurate time synchronization between heterogeneous sensors is crucial for ensuring robust state estimation in multi-sensor fusion systems. Sensor delays often cause discrepancies between the actual time when the event was captured and the time of sensor measurement, leading to temporal misalignment (time offset) between sensor measurement streams. In this paper, we propose an extended Kalman filter (EKF)-based radar-inertial odometry (RIO) framework that estimates the time offset online. The radar ego-velocity measurement model, estimated from a single radar scan, is formulated to include the time offset for the update. By leveraging temporal calibration, the proposed RIO enables accurate propagation and measurement updates based on a common time stream. Experiments on multiple datasets demonstrated the accurate time offset estimation of the proposed method and its impact on RIO performance, validating the importance of sensor time synchronization. Our implementation of the EKF-RIO with online temporal calibration is available at <https://github.com/spearwin/EKF-RIO-TC>.

Index Terms—Sensor Fusion, Localization, Radar, Temporal calibration

I. INTRODUCTION

Accurate and robust state estimation is crucial for the successful execution of autonomous missions using mobile robots or vehicles. Global navigation satellite system (GNSS) provides reliable estimation in typical outdoor environments, but its reliability degrades or it is unavailable in obstructed areas such as urban canyons or indoor environments. In such cases, alternative state estimation methods such as simultaneous localization and mapping (SLAM) or odometry using exteroceptive sensors (e.g., camera, LiDAR, and radar) are crucial to maintain reliable autonomy.

Over the past 20 years, real-time state estimation methods using light-based sensors such as a camera and a LiDAR have significantly improved accuracy and robustness in diverse environments [1]–[4]. Vision-based methods show notable performance across a wide range of conditions, despite

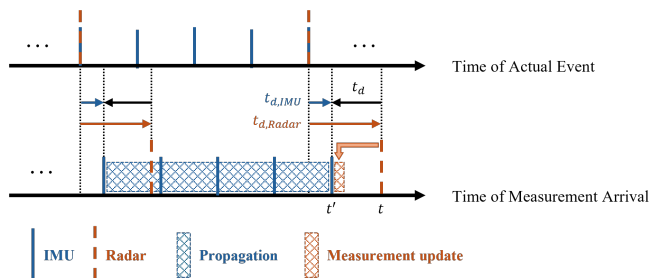


Fig. 1. Illustration of the temporal misalignment between IMU and radar measurement streams, along with the corresponding EKF’s propagation and measurement update steps. The time offset between the sensors is denoted as t_d . The time t' corresponds to the IMU measurement and t to the radar measurement.

relying on small and lightweight sensors. However, their performance significantly decreases in environments with lighting changes or visually featureless surfaces [5]. In contrast, LiDAR-based methods are resilient to lighting conditions, and can accurately capture the detailed structure of the surrounding environment over long distances. However, they struggle in environments with self-similarity, such as long corridors or structureless areas like flat planes [6]. Moreover, light-based sensors face limitations when exposed to small particles, such as snow, fog, or dust, due to their short wavelength.

Recently, a radar has gained attention as a promising solution to address these challenges [7]. In particular, a frequency-modulated continuous wave (FMCW) millimeter-wave 4D radar not only penetrates small particles effectively due to its relatively long wavelength but also measures relative speed (i.e., doppler velocity) to surrounding environments through frequency modulation. This radar typically operates at 5-20 Hz, providing raw signal data, 3D point clouds with spatial information and Doppler velocity for each point, enabling the estimation of ego-velocity from a single radar scan [8]. However, due to its relatively low sensor rate, it is necessary to predict the movement between consecutive radar scans. To address this, sensor fusion with an IMU, which operates at a higher sensor rate of over 100 Hz, can be utilized. The IMU complements the movement between consecutive radar scans, improving overall estimation accuracy and robustness. Therefore, there has been increasing interest and active research in radar-inertial odometry (RIO), which tightly couples the IMU with the radar.

*This research was supported by the Technology Innovation Program (No. 20018110, "Development of a wireless teleoperable relief robot for detecting searching and responding in narrow space") funded By the Ministry of Trade, Industry & Energy (MOTIE, Korea). (Corresponding author: Hyondong Oh)

¹Department of Mechanical Engineering, Ulsan National Institute of Science and Technology (UNIST), Ulsan 44919, Republic of Korea (e-mail: {pon02124; baegs94; oj7987; h.oh}@unist.ac.kr).

²Department of Electrical and Electronic Engineering, Imperial College London, SW7 2AZ London, United Kingdom (e-mail: sen.wang@imperial.ac.uk).

Accurate time synchronization between heterogeneous sensors is crucial for data fusion. All sensors inherently experience delays, leading to a discrepancy between the actual time when the event was captured and the time recorded as the sensor measurement, as illustrated in Fig. 1. While IMU systems typically have minimal latency, radar systems experience more significant delays due to factors such as signal processing steps, including fast Fourier transform, beamforming techniques, detection algorithms, and elevation angle estimation. Additionally, inherent hardware delays, including the analog-to-digital converter start-time and transmission delay, further contribute to the overall latency of radar systems [9]. Differences in sensor delays lead to temporal misalignments, which can pose significant challenges in multi-sensor systems. To address this issue, special hardware triggers or manufacturer software support may be required, but not all sensors provide such functions [10]. The time offset, which represents the difference in delays between IMU and radar systems, can reach up to hundreds of milliseconds, posing significant challenges for accurate data fusion in RIO. Compared with LiDAR-IMU and camera-IMU systems, our experimental results show that radar-IMU systems have a significantly larger time offset, highlighting the importance of temporal calibration.

In this paper, we propose a method for real-time estimation of the time offset between the IMU and the radar in an extended Kalman filter (EKF)-based RIO. Unlike existing RIO studies that rely on hardware/software triggers or do not consider the time offset, our method directly estimates the time offset online by utilizing the radar ego-velocity. The proposed method demonstrates efficient and robust performance across multiple datasets. Additionally, we show that accounting for the time offset in RIO enhances overall accuracy, even when using the same measurement model. The main contributions of this study can be summarized as:

- 1) We propose an EKF-RIO-TC framework that estimates the time offset between the IMU and the radar in real-time, utilizing the radar ego-velocity estimated from a single radar scan;
- 2) The proposed method is validated through both self-collected dataset from real-world environments and open datasets, with and without hardware triggers. The results show that the time offset between sensors is non-negligible and must be accurately estimated to improve RIO performance; and
- 3) To benefit the community, the implementation code has been made open-source. The proposed method is easy to implement and applicable, as it utilizes the radar ego-velocity measurement, which is commonly used in most RIO studies. To the best of our knowledge, this is the first work to implement online temporal calibration between sensors in RIO.

The remainder of this paper is organized as follows. Section II reviews the related work relevant to our research. Section III outlines notations used throughout the paper. Section IV details the framework of the proposed RIO,

accounting for the time offset between sensors. Section V validates the proposed method across multiple datasets and analyzes the results. Finally, Section VI summarizes the findings and concludes the paper.

II. RELATED WORK

In this section, we introduce filter-based RIO research using FMCW 4D radar. Because no existing research considers temporal calibration in the radar-IMU systems, we subsequently introduce research into online temporal calibration in other multi-sensor fusion systems.

A. Radar-Inertial Odometry with FMCW 4D Radars

Doer and Trommer [11] proposed an EKF-based RIO framework that fuses IMU data with 3D ego-velocity estimated from radar measurements. They introduced the 3-point RANSAC-LSQ to remove outliers from the noisy radar measurements during the ego-velocity estimation. Later, the same authors extended the filter state to include the extrinsic parameters between the IMU and the radar for online extrinsic estimation [12], and enhanced yaw estimation for indoor environments using Manhattan world assumptions [13]. Michalczyk et al. [14] focused on the relatively accurate radar measurements, specifically distance and Doppler velocity, utilizing them for filter updates. In addition to ego-velocity updates, they constructed point-to-point residuals between consecutive scans and leveraged the most informative dimension, which is distance, for the measurement update. The same authors extended this approach by incorporating multi-pose into the framework and including long-term observed points in the filter state to further improve performance [15]. Zhuang et al. [16] adopted graduated non-convexity for ego-velocity estimation and applied distribution-to-multi-distribution constraints for current scan and submap matching when utilizing point residuals for sparse radar points. They also incorporated scancontext for place revisits and loop closures via pose graphs. Kubelka et al. [10] compared scan matching-based methods (e.g., ICP, APD-GICP, and NDT) and radar ego-velocity-based methods (e.g., IMU attitude with radar ego-velocity and EKF-RIO [11]) across two distinct radar sensor setups. Scan matching-based methods showed better performance in dense point cloud setups, while radar ego-velocity-based methods excelled in sparse point cloud setups. In sparse radar setups, scan matching-based methods experienced random divergence due to incorrect scan matching caused by the low radar point cloud density. Performance degradation in radar ego-velocity-based methods was also observed in specific sections, such as when the vehicle hit a bump, causing discrepancies between the IMU and the radar measurements due to the temporal misalignment. Their analysis on this issue motivated our research.

In [11]–[13], hardware triggers were implemented on a microcontroller board for sensor time synchronization. In [10], and [14]–[16], the authors did not account for the time offset when constructing their system frameworks, assuming the times of sensor measurements were accurate.

Our proposed method estimates the time offset in real-time from radar ego-velocity, without relying on physical triggers. Since the ego-velocity is estimated from a single scan, there is no need for matching between consecutive scans, making the method independent of radar point cloud density, offering greater flexibility for various radar sensors. Furthermore, since all the mentioned works [10]–[16] utilize radar ego-velocity in the measurement update, the proposed method can be seamlessly integrated into their frameworks, not only ensuring accurate time synchronization but also potentially improving scan matching accuracy.

B. Online Temporal Calibration for Multi-Sensor Fusion Systems

Qin and Shen [17] proposed an optimization-based method for visual-inertial odometry (VIO) that enables online temporal calibration. They addressed time synchronization by jointly optimizing a prior factor, an IMU propagation factor, and a vision factor that accounts for the time offset between sensors. In particular, they compensated for feature measurements using the feature velocity on the image plane along with the time offset. Li and Mourikis [18] proposed a filter-based method to estimate the time offset between a camera and an IMU by including the time offset variable in the filter state. They formulated the camera measurement models for the 3D feature positions using the filter state including the time offset, thereby effectively estimating the time offset and improving the performance of VIO. Lee et al. [19] proposed a filter-based method for multi-sensor fusion odometry involving a LiDAR and an IMU. Since finding point correspondences between LiDAR scans can be challenging, they used plane patches, which contain structural information, to handle the data more efficiently. Their method involved extracting plane patches from the LiDAR point clouds and incorporating the time offset variable into the plane measurement models.

In contrast to previous works [17]–[19] which estimate the time offset by matching features between consecutive images or scans, our proposed method estimates the time offset from a single radar scan by formulating the radar ego-velocity measurement models. Unlike the camera and the LiDAR, the radar uniquely measures the Doppler velocity, enabling the direct estimation of ego-velocity. Instead of relying on scan matching, which can be challenging due to the sparse nature of radar point clouds, the proposed method avoids potential inaccuracies associated with correspondence matching.

III. NOTATION

Uppercase letters in superscripts (e.g., A in ${}^A\mathbf{q}_B$) denote the reference coordinate frame. Quaternions, which are commonly used to represent attitude, follow the Hamilton convention [20]. Vectors are represented by bold lowercase letters, matrices by bold uppercase letters, and scalars by non-bold lowercase letters.

${}^A\mathbf{q}_B$ represents the quaternion describing the attitude of frame B relative to frame A . The rotation matrix obtained from this quaternion, ${}^A\mathbf{R}_B = \mathbf{R}({}^A\mathbf{q}_B)$, is the part of

the special orthogonal group, $\text{SO}(3)$. ${}^A\mathbf{p}_B$ represents the position vector of frame B relative to frame A , expressed in the A frame.

IV. FILTER DESCRIPTION

The system is represented with three coordinate frames: the global frame G , the IMU frame I , and the radar frame R . The proposed EKF-based RIO aims to estimate the 6D pose of the IMU-fixed frame I with respect to the global reference frame G . The estimator utilizes the error state extended Kalman filter (ES-EKF), which is well-suited for handling the non-linear dynamics and measurement models typically encountered in pose estimation problems. By maintaining a minimal error-state and operating close to the origin, the ES-EKF avoids issues such as over-parameterization and singularities, ensuring consistency and efficiency. It also simplifies Jacobian computations, enhancing the filter’s robustness and computational efficiency when fusing IMU and radar measurements.

A. System Overview

Figure 1 illustrates the temporal misalignment between IMU and radar streams, along with the corresponding execution of EKF’s propagation and update steps. The upper plot shows the actual time when the event was captured by the sensors, while the lower plot represents the recorded time of the sensor measurement. Each sensor measures an actual event at a certain time, but due to delays (i.e., $t_{d,IMU}$ and $t_{d,Radar}$), the sensor measurement reflects a later time. The time offset t_d represents the difference between the delays of the IMU and the radar, defined as:

$$t_d = t_{d,IMU} - t_{d,Radar}. \quad (1)$$

Since the radar typically has a larger delay than the IMU, t_d generally takes a negative value.

Traditional EKF-based RIO performs propagation using IMU measurements until the radar measurement arrives, at which point the system executes the measurement update based on the times recorded in the sensor measurements. To ensure accurate state estimation, it is crucial to align the sensor measurements from both the IMU and the radar to a common time stream. While the exact delays of individual sensors are difficult to determine, the time offset t_d can be estimated in real-time using the radar ego-velocity, allowing the system to adjust the radar measurement to align with the IMU measurement time stream, which serves as the common time reference. By leveraging temporal calibration, the proposed RIO enables propagation and measurement updates to be performed based on a common time stream.

The system state and its representation are explained in Section IV-B. In Section IV-C, we cover the propagation using the IMU, and in Section IV-D, the radar measurement update is discussed. The online temporal calibration is detailed in Section IV-E.

B. System State

At time step k , the system state is defined as:

$$\mathbf{x}^k = \left({}^G\mathbf{q}_I^{k\top} \quad \mathbf{b}_g^{k\top} \quad {}^G\mathbf{v}_I^{k\top} \quad \mathbf{b}_a^{k\top} \quad {}^G\mathbf{p}_I^{k\top} \quad t_d^k \right)^\top, \quad (2)$$

where ${}^G\mathbf{q}_I$ represents the attitude, ${}^G\mathbf{v}_I$ the velocity, and ${}^G\mathbf{p}_I$ the position of the IMU. The terms \mathbf{b}_g and \mathbf{b}_a represent the gyroscope and accelerometer biases, respectively, and t_d represents the time offset defined in Eq. (1).

The error state formulation, as highlighted in [20], minimizes errors and avoids parameter singularities. Given the estimated state $\hat{\mathbf{x}}$ and the error state $\tilde{\mathbf{x}}$, the true state \mathbf{x} is expressed as:

$$\mathbf{x} = \hat{\mathbf{x}} + \tilde{\mathbf{x}}. \quad (3)$$

The true quaternion \mathbf{q} is represented as a combination of the estimated quaternion $\hat{\mathbf{q}}$ and the error quaternion $\tilde{\mathbf{q}}$ as $\mathbf{q} = \hat{\mathbf{q}} \otimes \tilde{\mathbf{q}}$, where \otimes denotes quaternion multiplication. The error quaternion $\tilde{\mathbf{q}}$ is approximated by $\tilde{\mathbf{q}} \approx \left[1 \quad \frac{1}{2}\boldsymbol{\theta}^\top \right]^\top$, with $\boldsymbol{\theta}$ representing a small Euler angle error.

Then, the error state at time step k is similarly defined as:

$$\tilde{\mathbf{x}}^k = \left({}^G\boldsymbol{\theta}_I^{k\top} \quad \tilde{\mathbf{b}}_g^{k\top} \quad {}^G\tilde{\mathbf{v}}_I^{k\top} \quad \tilde{\mathbf{b}}_a^{k\top} \quad {}^G\tilde{\mathbf{p}}_I^{k\top} \quad \tilde{t}_d^k \right)^\top. \quad (4)$$

For simplicity, the time index k is omitted in the following equations.

C. Propagation with IMU Measurements

The continuous-time dynamics for the estimated state is expressed as follows:

$$\begin{aligned} {}^G\dot{\hat{\mathbf{q}}}_I &= \frac{1}{2}\boldsymbol{\Omega}({}^I\hat{\boldsymbol{\omega}}_I){}^G\hat{\mathbf{q}}_I, & \dot{\hat{\mathbf{b}}}_g &= \mathbf{0}_{3 \times 1}, \\ {}^G\dot{\hat{\mathbf{v}}}_I &= {}^G\hat{\mathbf{R}}_I{}^I\hat{\mathbf{a}}_I + {}^G\mathbf{g}, & \dot{\hat{\mathbf{b}}}_a &= \mathbf{0}_{3 \times 1}, \\ {}^G\dot{\hat{\mathbf{p}}}_I &= {}^G\hat{\mathbf{v}}_I, & \dot{\hat{t}}_d &= 0, \end{aligned} \quad (5)$$

where ${}^G\mathbf{g}$ represents the gravity vector in the global frame. The estimated angular velocity ${}^I\hat{\boldsymbol{\omega}}_I$ and acceleration ${}^I\hat{\mathbf{a}}_I$ are expressed as ${}^I\hat{\boldsymbol{\omega}}_I = {}^I\boldsymbol{\omega}_I^m - \hat{\mathbf{b}}_g$ and ${}^I\hat{\mathbf{a}}_I = {}^I\mathbf{a}_I^m - \hat{\mathbf{b}}_a$, where ${}^I\boldsymbol{\omega}_I^m$ and ${}^I\mathbf{a}_I^m$ denote the gyroscope and accelerometer measurements, respectively, in the IMU frame. The matrix $\boldsymbol{\Omega}(\hat{\boldsymbol{\omega}})$, constructed from the estimated angular velocity $\hat{\boldsymbol{\omega}}$ and its skew-symmetric matrix $[\hat{\boldsymbol{\omega}} \times]$, is represented as:

$$\boldsymbol{\Omega}(\hat{\boldsymbol{\omega}}) = \begin{bmatrix} 0 & -\hat{\boldsymbol{\omega}}^\top \\ \hat{\boldsymbol{\omega}} & -[\hat{\boldsymbol{\omega}} \times] \end{bmatrix}. \quad (6)$$

The estimated state $\hat{\mathbf{x}}$ is propagated with IMU measurements through the continuous-time dynamics in Eq. (5), using 4th-order Runge-Kutta numerical integration.

For the covariance propagation, the linearized continuous-time dynamics for the error state is expressed as:

$$\dot{\tilde{\mathbf{x}}} = \mathbf{F}\tilde{\mathbf{x}} + \mathbf{G}\mathbf{n}, \quad (7)$$

where $\mathbf{n} = (\mathbf{n}_g^\top, \mathbf{n}_{wg}^\top, \mathbf{n}_a^\top, \mathbf{n}_{wa}^\top, n_d)^\top$. The noise vectors \mathbf{n}_g and \mathbf{n}_a represent the Gaussian noise affecting the gyroscope and accelerometer measurements, respectively. Similarly, \mathbf{n}_{wg} and \mathbf{n}_{wa} correspond to the random walks for the gyroscope and accelerometer measurement biases. The term

n_d accounts for the Gaussian noise (i.e., uncertainty) in the time offset.

The matrix \mathbf{F} represents the linearized system dynamics, and the matrix \mathbf{G} models the influence of the process noise on the error state. Only the non-zero elements of the matrix \mathbf{F} are given as follows:

$$\begin{aligned} \mathbf{F}(0 : 2, 0 : 2) &= -[({}^I\boldsymbol{\omega}_I^m - \hat{\mathbf{b}}_g) \times], \\ \mathbf{F}(0 : 2, 3 : 5) &= -\mathbf{I}_3, \\ \mathbf{F}(6 : 8, 0 : 2) &= -{}^G\hat{\mathbf{R}}_I [({}^I\mathbf{a}_I^m - \hat{\mathbf{b}}_a) \times], \\ \mathbf{F}(6 : 8, 9 : 11) &= -{}^G\hat{\mathbf{R}}_I, \\ \mathbf{F}(12 : 14, 6 : 8) &= \mathbf{I}_3. \end{aligned} \quad (8)$$

Similarly, the non-zero elements of the matrix \mathbf{G} are given as follows:

$$\begin{aligned} \mathbf{G}(0 : 2, 0 : 2) &= -\mathbf{I}_3, \\ \mathbf{G}(3 : 5, 3 : 5) &= \mathbf{I}_3, \\ \mathbf{G}(6 : 8, 6 : 8) &= -{}^G\hat{\mathbf{R}}_I, \\ \mathbf{G}(9 : 11, 9 : 11) &= \mathbf{I}_3, \\ \mathbf{G}(15, 12) &= 1. \end{aligned} \quad (9)$$

To propagate the covariance, the discrete-time state transition matrix Φ_k and discrete-time process noise covariance matrix \mathbf{Q}_k , derived from Eq. (7), are defined as follows:

$$\begin{aligned} \Phi_k &= \Phi(t_{k+1}, t_k) = \exp\left(\int_{t_k}^{t_{k+1}} \mathbf{F}(\tau) d\tau\right), \\ \mathbf{Q}_k &= \int_{t_k}^{t_{k+1}} \Phi(t_{k+1}, \tau) \mathbf{G} \mathbf{Q} \mathbf{G}^\top \Phi(t_{k+1}, \tau)^\top d\tau, \end{aligned} \quad (10)$$

where \mathbf{Q} is the continuous-time process noise covariance matrix. The propagated covariance matrix is expressed as:

$$\mathbf{P}_{k+1|k} = \Phi_k \mathbf{P}_{k|k} \Phi_k^\top + \mathbf{Q}_k. \quad (11)$$

Considering the time offset t_d , propagation is repeated up to just before the time of the radar measurement aligned to the IMU measurement time stream.

D. Measurement Update with Radar Measurements

The FMCW 4D radar provides 3D point clouds, where each point includes a 3D position and a scalar Doppler velocity. The Doppler velocity represents the radial velocity of a target point, expressed as:

$$v_d^i = -{}^R\mathbf{v}_R \cdot \frac{{}^R\mathbf{p}_f^i}{\|{}^R\mathbf{p}_f^i\|}, \quad \text{for } i = 1, \dots, N, \quad (12)$$

where N is the total number of detected points, v_d^i denotes the Doppler velocity of the i -th point, ${}^R\mathbf{p}_f^i$ is the position vector of the i -th point in the radar frame, and ${}^R\mathbf{v}_R$ denotes the radar ego-velocity. To estimate the radar ego-velocity ${}^R\mathbf{v}_R$ from noisy radar measurements, various methods, such as RANSAC and m-estimator-based optimization, have been proposed. In this work, we adopt the 3-point RANSAC-LSQ [11], a simple yet robust method that efficiently eliminates outliers and estimates the radar ego-velocity ${}^R\mathbf{v}_R$, which is used in the measurement update.

In the case where the IMU and radar are rigidly connected, the radar ego-velocity measurement model can be expressed using the system state. As derived in [11], the radar ego-velocity is expressed as:

$${}^R\mathbf{v}_R(t) = {}^R\mathbf{R}_I \left({}^G\mathbf{R}_I^\top(t) {}^G\mathbf{v}_I(t) + [({}^I\boldsymbol{\omega}_I^m(t) - \mathbf{b}_g(t)) \times] {}^I\mathbf{p}_R \right), \quad (13)$$

where the extrinsic parameters, ${}^R\mathbf{R}_I$ and ${}^I\mathbf{p}_R$, between the IMU and the radar are assumed to be pre-calibrated and constant.

In the measurement update, the residual \mathbf{r} is computed as the difference between the radar ego-velocity ${}^R\mathbf{v}_R$, estimated from the radar measurements, and the predicted radar ego-velocity ${}^R\hat{\mathbf{v}}_R$ from the state. The residual is expressed as:

$$\mathbf{r} = {}^R\mathbf{v}_R(t) - {}^R\hat{\mathbf{v}}_R(t) = \mathbf{h}(\tilde{\mathbf{x}}) + \mathbf{n}_r. \quad (14)$$

As illustrated in Fig. 1, $t' = t + t_d$ represents the IMU measurement time, which serves as the reference time stream in the filter, while t represents the radar measurement time used in the measurement update after being aligned to the IMU time stream. The term \mathbf{n}_r denotes the noise of the measurement. The function $\mathbf{h}(\tilde{\mathbf{x}})$ is a nonlinear function that relates the state error $\tilde{\mathbf{x}}$ to the radar ego-velocity measurement residual. For use in the EKF, this function is linearized with respect to the system state. The measurement Jacobian matrix \mathbf{H} is expressed as follows:

$$\begin{aligned} \mathbf{H} &= [\mathbf{H}_q \quad \mathbf{H}_{b_g} \quad \mathbf{H}_v \quad \mathbf{0}_{3 \times 3} \quad \mathbf{0}_{3 \times 3} \quad \mathbf{H}_{t_d}], \\ \mathbf{H}_q &= {}^R\mathbf{R}_I [{}^G\hat{\mathbf{R}}_I^\top {}^G\hat{\mathbf{v}}_I \times], \\ \mathbf{H}_{b_g} &= {}^R\mathbf{R}_I [{}^I\mathbf{p}_R \times], \\ \mathbf{H}_v &= {}^R\mathbf{R}_I {}^G\hat{\mathbf{R}}_I^\top. \end{aligned} \quad (15)$$

In Eq. (13), the time-varying states are ${}^G\mathbf{R}_I$ and ${}^G\mathbf{v}_I$. By applying the chain rule, the Jacobian \mathbf{H}_{t_d} is expressed as:

$$\begin{aligned} \mathbf{H}_{t_d} &= \frac{\partial \mathbf{h}(\tilde{\mathbf{x}}(t'))}{\partial {}^G\boldsymbol{\theta}_I(t')} \cdot \frac{\partial {}^G\boldsymbol{\theta}_I(t')}{\partial t'} \cdot \frac{\partial t'}{\partial t_d} \\ &+ \frac{\partial \mathbf{h}(\tilde{\mathbf{x}}(t'))}{\partial {}^G\tilde{\mathbf{v}}_I(t')} \cdot \frac{\partial {}^G\tilde{\mathbf{v}}_I(t')}{\partial t'} \cdot \frac{\partial t'}{\partial t_d} \\ &= \mathbf{H}_q \left({}^G\hat{\mathbf{R}}_I(t') \left({}^I\boldsymbol{\omega}_I^m(t') - \hat{\mathbf{b}}_g(t') \right) \right) \\ &+ \mathbf{H}_v \left({}^G\hat{\mathbf{R}}_I(t') \left({}^I\mathbf{a}_I^m(t') - \hat{\mathbf{b}}_a(t') \right) + {}^G\mathbf{g} \right). \end{aligned} \quad (16)$$

The EKF update proceeds by computing the Kalman gain \mathbf{K} as:

$$\mathbf{K} = \mathbf{P}_{k+1|k} \mathbf{H}^\top (\mathbf{H} \mathbf{P}_{k+1|k} \mathbf{H}^\top + \mathbf{R})^{-1}, \quad (17)$$

where \mathbf{R} represents the measurement noise covariance matrix. Finally, the estimated state and covariance are updated according to the Kalman gain as follows:

$$\begin{aligned} \hat{\mathbf{x}}_{k+1|k+1} &= \hat{\mathbf{x}}_{k+1|k} + \mathbf{K}\mathbf{r}, \\ \mathbf{P}_{k+1|k+1} &= (\mathbf{I} - \mathbf{K}\mathbf{H}) \mathbf{P}_{k+1|k}. \end{aligned} \quad (18)$$

Each time new radar measurement is received, the measurement update is performed based on the IMU time stream.

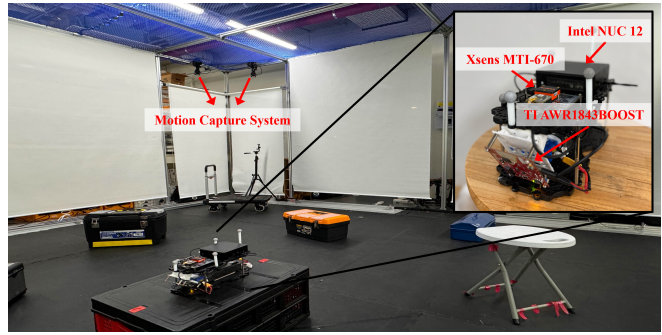


Fig. 2. The handheld platform configuration, including the radar, IMU, and onboard computer. The experiments are conducted in a room equipped with a motion capture system to obtain accurate ground truth.

E. Online Temporal Calibration

The proposed method estimates the time offset between the IMU and the radar in real-time by employing the radar ego-velocity measurement model. By accounting for the time offset, the proposed method ensures that both propagation and measurement updates are performed based on a common time stream, ensuring that the measurements from both sensors are synchronized.

The time offset is propagated using a noise model n_d , as described in Eq. (7). If the time offset is constant over time or approximately known, it can be estimated without a noise model. However, the time offset varies across sensor models, making it difficult to predefine in most cases. Furthermore, when the vehicle is moving slowly, the impact of the time offset becomes less significant, making it harder to estimate. For this reason, the time offset is modeled as a random walk.

In the measurement model presented in Eq. (13), the factors affected by the temporal misalignment between sensors are not only the state variables ${}^G\mathbf{R}_I$, ${}^G\mathbf{v}_I$, and \mathbf{b}_g , but also the gyroscope measurement ${}^I\boldsymbol{\omega}_I^m$. Although \mathbf{b}_g , which does not change significantly over time, is negligible, failing to account for the time offset causes the state to propagate over a misaligned time stream, leading to errors in the estimates of ${}^G\mathbf{R}_I$ and ${}^G\mathbf{v}_I$. Moreover, the improper use of the gyroscope measurement further degrades the estimation accuracy, and this error accumulates over time. Therefore, accounting for the time offset is crucial to maintain the accuracy and consistency of the state estimates.

V. EXPERIMENTS

A. Experimental Setup

We conduct experiments using three datasets, comprising a total of 15 sequences. One is our self-collected dataset, captured with a handheld platform as shown in Fig. 2, while the other two are public radar datasets: ICINS2021 [13], and ColoRadar [21]. The sensors on our platform include a 4D FMCW radar, specifically the Texas Instruments AWR1843BOOST, and an Xsens MTI-670-DK IMU. No additional hardware triggers are used between the sensors, and the sensor data is recorded using an Intel NUC i7 onboard computer. The experiments are conducted in an

TABLE I

QUANTITATIVE RESULTS OF FIXED OFFSET AND ONLINE ESTIMATION

Sequence	Method	Time Offset (s)	APE RMSE		RPE RMSE	
			Trans. (m)	Rot. (°)	Trans. (m)	Rot. (°)
Sequence 1	Fixed Offset	0.0	0.985	1.872	0.264	1.230
		-0.05	0.647	7.561	0.166	1.549
		-0.10	0.661	2.438	0.138	0.948
		-0.15	0.826	5.151	0.131	1.196
		-0.20	0.974	2.698	0.156	1.274
	Online Est.	-0.114	0.646	0.935	0.132	0.774
Sequence 4	Fixed Offset	0.0	1.737	25.885	0.118	4.074
		-0.05	1.028	15.460	0.091	2.313
		-0.10	0.635	4.655	0.061	0.994
		-0.15	0.649	4.275	0.068	1.083
		-0.20	0.716	12.461	0.092	2.526
	Online Est.	-0.115	0.610	3.099	0.057	0.944

*The initial time offset of ‘Online Est.’ is set to 0.0 and the converged values are shown above.

**For each sequence, the lowest error values among the fixed offsets are highlighted in red, and the second-lowest in blue.

indoor area equipped with a motion capture system to obtain precise ground truth. The extrinsic calibration between the IMU and the radar is performed manually. To highlight the significance of temporal calibration in RIO, we design the dataset with two levels of difficulty. Sequences 1 to 3 feature standard motion patterns, while Sequences 4 to 7 introduce more rotational motion to induce larger errors due to the time offset, providing a clearer demonstration of its impact.

In [13], the ICINS2021 dataset is collected using a Texas Instruments IWR6843AOP radar sensor, an Analog Devices ADIS16448 IMU sensor, and a camera. A micro-controller board is used for active hardware triggering to accurately capture the timing of the radar measurements. Data is collected using both handheld and drone platforms. The handheld sequences, “carried_1” and “carried_2”, are referred to as “ICINS 1” and “ICINS 2”, while the drone sequences, “flight_1” and “flight_2”, are referred to as “ICINS 3” and “ICINS 4”, respectively. The ground truth is provided through visual-inertial SLAM, which performs multiple loop closures, offering a pseudo-ground truth. In [21], the ColoRadar dataset is collected using a Texas Instruments AWR1843BOOST radar sensor, a Microstrain 3DM-GX5-25 IMU sensor, and a LiDAR mounted on a handheld platform. No specific synchronization setup is used between the sensors. The sequences, “arpg_lab_run0” and “arpg_lab_run1”, are referred to as “ColoRadar 1” and “ColoRadar 2”, while the sequences “ec_hallways_run0” and “ec_hallways_run1” are referred to as “ColoRadar 3” and “ColoRadar 4”, respectively. The ground truth is generated via LiDAR-inertial SLAM, which includes loop closures, offering a pseudo-ground truth.

B. Evaluation

For the performance comparison, the open-source EKF-RIO [11], which uses the same measurement model but does not account for temporal calibration, is employed. All parameters are kept identical to ensure a fair comparison. In the proposed method, the time offset t_d is initialized to

0.0 seconds for all sequences, reflecting a typical scenario where the initial time offset is unknown. The experimental results are evaluated using the open-source tool EVO [22]. Figure 3 illustrates the estimated trajectories compared to the ground truth for visual comparison, with one representative result from each dataset. Due to the stochastic nature of the RANSAC algorithm used in radar ego-velocity estimation, the averaged results from 100 trials across all datasets are presented. We compare the root mean square error (RMSE) of both absolute pose error (APE) and relative pose error (RPE), with the RPE calculated at 10-meter intervals.

APE evaluates the overall trajectory by calculating the difference between the ground truth and the estimated poses for all frames, making it particularly useful for assessing the global accuracy of the estimated trajectory. However, APE can be sensitive to significant rotational errors that occur early or in specific sections, potentially overshadowing smaller errors later in the trajectory. In contrast, RPE focuses on local accuracy by aligning poses at regular intervals and calculating the error, allowing discrepancies over shorter segments to be highlighted. When the temporal calibration between sensors is not accounted for, errors can accumulate over time, making RPE evaluation essential. Both metrics offer valuable insights, providing a comprehensive evaluation of the trajectory.

1) *Self-Collected Dataset:* The purpose of the self-collected dataset is to identify the actual time offset between the IMU and the radar and evaluate its impact on the accuracy of RIO. Since the handheld platform does not utilize a hardware trigger to synchronize the sensors, the exact time offset is unknown and must be estimated. To address this uncertainty, we evaluate the performance of fixed time offsets over a range of values to determine the interval that provides the best accuracy and estimate the likely time offset range.

As shown in Table I, error values are analyzed with fixed offsets set at 0.05-second intervals for both Sequence 1 and Sequence 4, which feature different motion patterns. The results show that the time offset falls within the -0.10 to -0.15 second range, where the highest accuracy in terms of APE and RPE is observed for both sequences. The proposed method, which utilizes online temporal calibration, estimates the time offset as -0.114 seconds for Sequence 1 and -0.115 seconds for Sequence 4, closely matching the range found through fixed offset testing. In both cases, the proposed method achieves improved performance in terms of both APE and RPE, demonstrates its effectiveness in accurately estimating the time offset.

Since the radar delay is generally larger than IMU delay, the time offset t_d , representing the difference between these delays, typically takes a negative value. To evaluate the robustness of the estimation, different initial values of t_d ranging from 0.0 to -0.3 seconds are tested. Figure 4 illustrates the estimated time offset for each initial setting, along with the 3-sigma boundaries. As t_d is estimated from radar ego-velocity, it cannot be determined while the platform is stationary. Once the platform starts moving, the filter begins estimating t_d and quickly converges to a stable value.

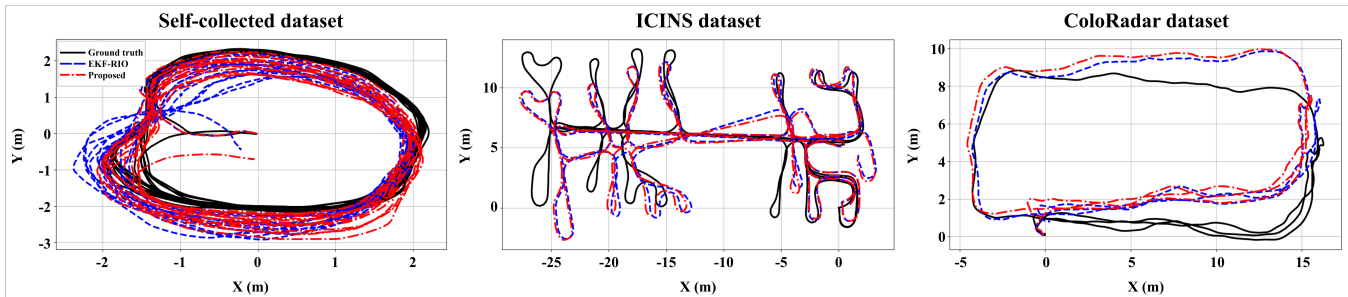


Fig. 3. Comparison of estimated trajectories with the ground truth. The black trajectory is the ground truth, the blue one is the EKF-RIO, which does not account for temporal calibration, and the red one is the proposed RIO with online temporal calibration. Results are presented for Sequence 4, ICINS 1, and ColoRadar 1, representing one sequence from each of the three datasets.

TABLE II
QUANTITATIVE RESULTS OF COMPARISON STUDY ON SELF-COLLECTED DATASET

Sequence (Trajectory Length)	Method (\hat{t}_d)	APE RMSE		RPE RMSE	
		Trans. (m)	Rot. ($^\circ$)	Trans. (m)	Rot. ($^\circ$)
Sequence 1 (177 m)	EKF-RIO (N/A)	0.985	1.872	0.264	1.230
	Ours (-0.114 s)	0.646	0.935	0.132	0.774
Sequence 2 (197 m)	EKF-RIO	2.269	2.161	0.136	1.414
	Ours (-0.114 s)	0.587	1.650	0.064	0.774
Sequence 3 (144 m)	EKF-RIO	1.368	2.331	0.167	1.347
	Ours (-0.113 s)	0.414	1.140	0.088	0.613
Sequence 4 (197 m)	EKF-RIO	1.737	25.885	0.118	4.074
	Ours (-0.115 s)	0.610	3.099	0.057	0.944
Sequence 5 (190 m)	EKF-RIO	2.375	7.702	0.122	1.600
	Ours (-0.115 s)	1.150	1.304	0.069	0.814
Sequence 6 (179 m)	EKF-RIO	1.267	17.907	0.117	2.828
	Ours (-0.111 s)	0.661	2.551	0.051	0.809
Sequence 7 (223 m)	EKF-RIO	2.757	10.092	0.116	1.863
	Ours (-0.112 s)	1.596	6.039	0.057	1.365
Average	Ours (-0.113 s)	1.822	9.707	0.148	2.051
	Ours (-0.113 s)	0.809	2.388	0.074	0.870

The filter converges to a stable time offset of -0.114 ± 0.001 seconds in Sequence 1 and -0.115 ± 0.001 seconds in Sequence 4.

Table II presents the performance comparison between the proposed method with online temporal calibration and EKF-RIO across seven sequences. The proposed method outperforms EKF-RIO, significantly reducing both APE and RPE across all sequences. Specifically, it reduces APE translation error by an average of 56%, APE rotation error by 75%, RPE translation error by 50%, and RPE rotation error by 58% compared with EKF-RIO. Despite using the same measurement model, the performance improvement is achieved solely by applying propagation and updates based on a common time stream through the proposed online temporal calibration.

On average, the time offset t_d is estimated to be -0.113 ± 0.002 seconds, confirming consistent temporal calibration throughout the experiments. Compared with LiDAR-inertial and visual-inertial systems, radar-inertial systems exhibit a significantly larger time offset, as shown in Table III. Given the radar sensor rate (10 Hz), such a large time offset is significant enough to cause a misalignment spanning more

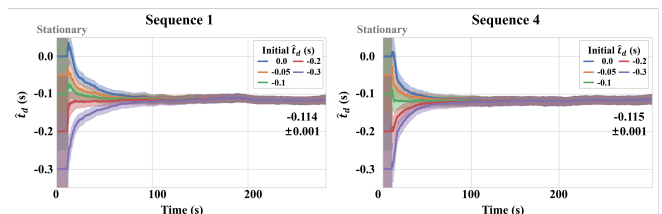


Fig. 4. Time offset estimation with 3-sigma boundaries for different initial values in Sequence 1 and 4.

TABLE III
COMPARISON OF TIME OFFSET IN MULTI-SENSOR FUSION SYSTEMS

Systems	Sensor	Time Offset
LiDAR-Inertial [23]	Velodyne VLP-32	0.006 s
Visual-Inertial [18]	PointGrey Bumblebee2	0.047 s
Radar-Inertial	TI AWR1843BOOST	0.113 s

than one data frame. These findings highlight the necessity of temporal calibration in RIO, which is crucial for accurate sensor fusion and reliable pose estimation in real-world applications.

2) *Open Datasets*: Table IV presents the results from the two open datasets. The ICINS dataset incorporates a hardware trigger for the radar, which we use to validate the accuracy of the time offset estimation for the proposed method. In this setup, a microcontroller sends radar trigger signals, prompting the radar to begin scanning. The radar data is timestamped based on the actual trigger signal, providing a pseudo-ground truth for time offset estimation. Theoretically, if the sensors are time-synchronized through triggers, the time offset t_d is expected to be close to 0.0 seconds. The proposed method estimates the time offset to be an average of 0.016 ± 0.003 seconds. Despite this slight discrepancy, the proposed method demonstrates comparable or improved performance on average in both APE and RPE compared with EKF-RIO. Although the ICINS dataset includes hardware-triggered signals for the radar, there is no such trigger signal for the IMU in the dataset, which may introduce a delay in IMU measurements. As defined in Eq. (1), we attribute the estimated positive time offset to this IMU delay, explaining the difference from the expected value.

TABLE IV

QUANTITATIVE RESULTS OF COMPARISON STUDY ON OPEN DATASETS

Sequence (Trajectory Length)	Method (t_d)	APE RMSE		RPE RMSE	
		Trans. (m)	Rot. ($^\circ$)	Trans. (m)	Rot. ($^\circ$)
ICINS 1 (295 m)	EKF-RIO (N/A)	1.959	10.694	0.093	0.896
	Ours (0.016 s)	1.922	10.135	0.098	0.918
ICINS 2 (468 m)	EKF-RIO	3.830	23.151	0.114	1.289
	Ours (0.013 s)	3.198	19.235	0.121	1.076
ICINS 3 (150 m)	EKF-RIO	1.502	9.905	0.130	1.512
	Ours (0.015 s)	1.530	10.189	0.126	1.553
ICINS 4 (50 m)	EKF-RIO	0.213	2.091	0.076	0.923
	Ours (0.019 s)	0.216	2.098	0.081	0.923
Average	EKF-RIO	1.876	11.460	0.103	1.155
	Ours (0.016 s)	1.716	10.414	0.106	1.117
ColoRadar 1 (178 m)	EKF-RIO (N/A)	6.556	1.354	0.182	1.071
	Ours (-0.110 s)	6.173	1.382	0.155	1.188
ColoRadar 2 (197 m)	EKF-RIO	4.747	1.238	0.372	1.375
	Ours (-0.114 s)	4.826	0.960	0.292	1.180
ColoRadar 3 (197 m)	EKF-RIO	8.307	1.969	0.259	1.015
	Ours (-0.108 s)	8.550	1.852	0.221	0.879
ColoRadar 4 (144 m)	EKF-RIO	12.111	2.815	0.488	1.263
	Ours (-0.112 s)	11.946	2.756	0.200	1.116
Average	EKF-RIO	7.930	1.844	0.325	1.181
	Ours(-0.111 s)	7.874	1.737	0.217	1.091

The ColoRadar dataset, widely used for performance comparison in the RIO field, is utilized to assess if the proposed method generalizes well across different datasets. As shown in Table IV, the proposed method also demonstrates performance improvements over EKF-RIO in terms of both APE and RPE on average. However, the extent of improvement is smaller compared with the self-collected dataset, which can be explained by differences in trajectory characteristics. The radar ego-velocity model utilizes not only the accelerometer but also the gyroscope measurements. As illustrated in Fig. 3, the ColoRadar dataset involves movement over a larger area with less rotation, leading to a smaller impact of the time offset on performance. Nonetheless, the proposed method achieves 33% reduction in RPE translation error, demonstrating its effectiveness even in this less challenging trajectory. On average, the time offset t_d is estimated to be -0.111 ± 0.003 seconds, similar to the time offset found in the self-collected dataset. This consistency is likely due to the use of the same radar sensor model in both datasets, further validating the reliability of the proposed method across different environments.

VI. CONCLUSIONS AND FUTURE WORK

In this paper, we proposed an EKF-based RIO framework with online temporal calibration. To ensure accurate sensor time synchronization during IMU and radar sensor fusion, the time offset between sensors is estimated from radar ego-velocity, which is derived from a single radar scan. This approach avoids the potential risks of finding correspondences between consecutive radar scans and, being independent of radar point cloud density, offers flexibility for use with various types of radar sensors. By leveraging temporal calibration, sensor measurements are aligned to a

common time stream. This allows propagation and measurement updates to be applied at the correct time, improving overall performance. Extensive experiments across multiple datasets demonstrate the effectiveness of time offset estimation and provide a detailed analysis of its impact on overall performance.

Several challenges remain in multi-sensor fusion state estimation using radar systems. One issue is the reliance on manually calibrated sensor extrinsic parameters in many studies, which can lead to inaccuracies. We will focus on spatiotemporal calibration between sensors to further improve the accuracy and robustness of multi-sensor fusion systems.

REFERENCES

- [1] P. Geneva, K. Eickenhoff, W. Lee, Y. Yang, and G. Huang, "OpenVINS: A Research Platform for Visual-Inertial Estimation," in *IEEE International Conference on Robotics and Automation*, 2020, pp. 4666–4672.
- [2] C. Campos, R. Elvira, J. J. G. Rodríguez, J. M. M. Montiel, and J. D. Tardós, "ORB-SLAM3: An Accurate Open-Source Library for Visual, Visual-Inertial, and Multimap SLAM," *IEEE Transactions on Robotics*, vol. 37, no. 6, pp. 1874–1890, 2021.
- [3] T. Shan, B. Englot, D. Meyers, W. Wang, C. Ratti, and D. Rus, "LIO-SAM: Tightly-coupled Lidar Inertial Odometry via Smoothing and Mapping," in *IEEE/RSJ International Conference on Intelligent Robots and Systems*, 2020, pp. 5135–5142.
- [4] W. Xu, Y. Cai, D. He, J. Lin, and F. Zhang, "FAST-LIO2: Fast Direct LiDAR-Inertial Odometry," *IEEE Transactions on Robotics*, vol. 38, no. 4, pp. 2053–2073, 2022.
- [5] J. Zhang and S. Singh, "Laser-visual-inertial odometry and mapping with high robustness and low drift," *Journal of Field Robotics*, vol. 35, no. 8, pp. 1242–1264, 2018.
- [6] M. Nissav, N. Khedekar, and K. Alexis, "Degradation Resilient LiDAR-Radar-Inertial Odometry," in *IEEE International Conference on Robotics and Automation*, 2024, pp. 8587–8594.
- [7] K. Harlow, H. Jang, T. D. Barfoot, A. Kim, and C. Heckman, "A New Wave in Robotics: Survey on Recent MmWave Radar Applications in Robotics," *IEEE Transactions on Robotics*, vol. 40, pp. 4544–4560, 2024.
- [8] D. Kellner, M. Barjenbruch, J. Klappstein, J. Dickmann, and K. Dietmayer, "Instantaneous ego-motion estimation using Doppler radar," in *IEEE Conference on Intelligent Transportation Systems*, 2013, pp. 869–874.
- [9] L. Fan, J. Wang, Y. Chang, Y. Li, Y. Wang, and D. Cao, "4D mmWave Radar for Autonomous Driving Perception: A Comprehensive Survey," *IEEE Transactions on Intelligent Vehicles*, vol. 9, no. 4, pp. 4606–4620, 2024.
- [10] V. Kubelka, E. Fritz, and M. Magnusson, "Do we need scan-matching in radar odometry?" in *IEEE International Conference on Robotics and Automation*, 2024, pp. 13710–13716.
- [11] C. Doer and G. F. Trommer, "An EKF Based Approach to Radar Inertial Odometry," in *IEEE International Conference on Multisensor Fusion and Integration for Intelligent Systems*, 2020, pp. 152–159.
- [12] C. Doer and G. F. Trommer, "Radar Inertial Odometry With Online Calibration," in *European Navigation Conference*, 2020, pp. 1–10.
- [13] C. Doer and G. F. Trommer, "Yaw aided Radar Inertial Odometry using Manhattan World Assumptions," in *International Conference on Integrated Navigation Systems*, 2021, pp. 1–9.
- [14] J. Michalczyk, R. Jung, and S. Weiss, "Tightly-Coupled EKF-Based Radar-Inertial Odometry," in *IEEE/RSJ International Conference on Intelligent Robots and Systems*, 2022, pp. 12336–12343.
- [15] J. Michalczyk, R. Jung, C. Brommer, and S. Weiss, "Multi-State Tightly-Coupled EKF-Based Radar-Inertial Odometry With Persistent Landmarks," in *IEEE International Conference on Robotics and Automation*, 2023, pp. 4011–4017.
- [16] Y. Zhuang, B. Wang, J. Huai, and M. Li, "4D iRIOM: 4D Imaging Radar Inertial Odometry and Mapping," *IEEE Robotics and Automation Letters*, vol. 8, no. 6, pp. 3246–3253, 2023.
- [17] T. Qin and S. Shen, "Online Temporal Calibration for Monocular Visual-Inertial Systems," in *IEEE/RSJ International Conference on Intelligent Robots and Systems*, 2018, pp. 3662–3669.

- [18] M. Li and A. I. Mourikis, "Online temporal calibration for camera-IMU systems: Theory and algorithms," *The International Journal of Robotics Research*, vol. 33, no. 7, pp. 947-964, 2014.
- [19] W. Lee, Y. Yang, and G. Huang, "Efficient Multi-sensor Aided Inertial Navigation with Online Calibration," in *IEEE International Conference on Robotics and Automation*, 2021, pp. 5706-5712.
- [20] J. Sola, "Quaternion kinematics for the error-state Kalman filter," *arXiv preprint arXiv:1711.02508*, 2017.
- [21] A. Kramer, K. Harlow, C. Williams, and C. Heckman, "ColoRadar: The direct 3D millimeter wave radar dataset," *The International Journal of Robotics Research*, vol. 41, no. 4, pp. 351-360, 2022.
- [22] M. Grupp, "evo: Python package for the evaluation of odometry and SLAM," <https://github.com/MichaelGrupp/evo>, 2017.
- [23] S. Li, X. Li, S. Chen, Y. Zhou, and S. Wang, "Two-step LiDAR/Camera/IMU spatial and temporal calibration based on continuous-time trajectory estimation," *IEEE Transactions on Industrial Electronics*, vol. 71, no. 3, pp. 3182-3191, 2024.